Optimal nose shaping for delayed boundary-layer separation in laminar plane-symmetric and axisymmetric flow

T. W. Mattner, E. O. Tuck & J. P. Denier

School of Mathematical Sciences
The University of Adelaide, SA, 5005 AUSTRALIA

Abstract

The aim of this work is to design a forebody of minimum overall length that nevertheless allows laminar unseparated flow. This design goal is formulated as a constrained optimization problem. Classical potential and boundary-layer flow solvers are combined with the Feasible Direction Interior Point optimization algorithm to obtain representative forebody geometries in plane-symmetric and axisymmetric flow. The optimal forebody shape consists of an essentially flat plate normal to the flow, connected to the aftbody by a smooth zero shear-stress surface.

Introduction

We consider constant-density incompressible steady viscous laminar flow past plane-symmetric and axisymmetric bodies at zero angle of incidence (i.e., the axis or plane of symmetry is aligned with the flow). The aft section of the body is a constant-thickness plate or constant-diameter cylinder that is either of infinite length, or (as is the case in this paper) sufficiently long that details of how the geometry is terminated only weakly affect the upstream flow. If the forward section of the body (forebody) is too short or improperly shaped, forebody boundary-layer separation will occur. Separation is usually undesirable, yet it is sometimes necessary to make the forebody as short as possible. Our aim is to design a forebody of minimum overall length that nevertheless allows unseparated flow.

Let the position vector of a point on the forebody be $\mathbf{X}(s) = (X(s), Y(s))$, where s is the arclength measured from the axis of symmetry, $\mathbf{X}(0) = (-L, 0)$, $\mathbf{X}(s_0) = (0, D/2)$, and the fore/aftbody junction is located at $s = s_0$ (Figure 1). The objective is to

$$\text{minimize} \quad f(\mathbf{X}) = -X(0) = L \quad (1)$$

subject to

$$g_A(\mathbf{X}) = -\tau(s) \leq 0, \quad 0 \leq s \leq s_0, \quad (2)$$

where τ is the surface shear stress. The objective function is linear, hence the solution lies on a boundary defined by the constraints and will exhibit a point or region of incipient separation, that is, zero shear stress. In general, the constraint permits nonconvex geometry. In this paper, the geometry is restricted by imposing the secondary constraint

$$g_B(\mathbf{X}) = -\frac{dX}{ds} = -X_s \leq 0, \quad 0 \leq s \leq s_0, \quad (3)$$

thus excluding hollow-nosed geometry ($X(s) < X(0)$ for some $s > 0$), while permitting lobed geometry ($Y(s) > Y(s_0)$ for some $s < s_0$). A more restrictive constraint on the curvature, $-\kappa(s) \leq 0$, would explicitly enforce convex geometry.

Numerical methods

Geometry

The aftbody geometry is a finite-length enclosed body consisting of a flat plate (cylinder) terminated by a semicircular (hemispherical) end-cap. Cubic splines (with appropriate symmetry
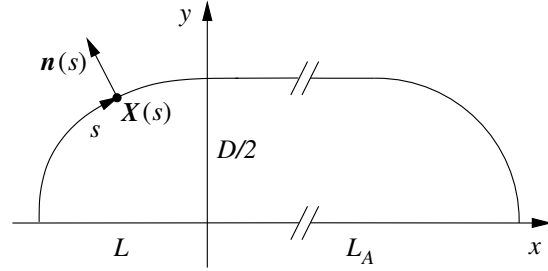

Figure 1: Geometry definition. The x-axis is the plane or axis of symmetry.

conditions) are used to represent the geometry and compute the arclength, s, surface normal $\mathbf{n}(s) = (n_x, n_y)$, and curvature, $\kappa(s)$.

Potential flow

In this paper, it is assumed that viscous effects are confined to the boundary layer. Outside the boundary layer, the flow is effectively inviscid and described by a velocity potential satisfying the Laplace equation. The external velocity potential is obtained using interior point (ring) sources [1] and is given by

$$\phi(x, y) = U_\infty x + \sum_{j=1}^{N} m_j \Phi(x, \hat{X}_j, y, \hat{Y}_j) \quad (4)$$

where U_∞ is a uniform far-field velocity, N is the number of point (ring) sources, m_j and $(\hat{X}_j, \hat{Y}_j)$ are the strength and coordinates of the j-th source, respectively, and

$$\Phi(x, x_0, y, y_0) = \log[(x - x_0)^2 + (y - y_0)^2]^{1/2} \quad (5)$$
$$+ \log[(x - x_0)^2 + (y + y_0)^2]^{1/2} \quad (6)$$

for plane-symmetric flow, or

$$\Phi(x, x_0, y, y_0) = \frac{K(k)}{[(x - x_0)^2 + (y + y_0)^2]^{1/2}} \quad (7)$$

for axisymmetric flow. Here, K is the complete elliptic integral of the first kind and

$$k^2 = \frac{4yy_0}{(x - x_0)^2 + (y + y_0)^2}. \quad (8)$$

Applying the no-penetration boundary condition $\nabla \phi \cdot \mathbf{n}$ at N discrete points on the body surface yields the linear system

$$\sum_{j=1}^{N} \left[n_x(s_i) \frac{\partial \Phi}{\partial x}(X_i, \hat{X}_j, Y_i, \hat{Y}_j) + n_y(s_i) \frac{\partial \Phi}{\partial y}(X_i, \hat{X}_j, Y_i, \hat{Y}_j) \right] m_j$$
$$= -U_\infty n_x(s_i), \quad i = 1, \ldots, N, \quad (9)$$

where $\mathbf{X}(s_i) = (X_i, Y_i)$ is the i-th node. The point (ring) source locations are given by $\hat{X}_j = X_j - \gamma \Delta s\, n_x(s_j)$ and $\hat{Y}_j =$
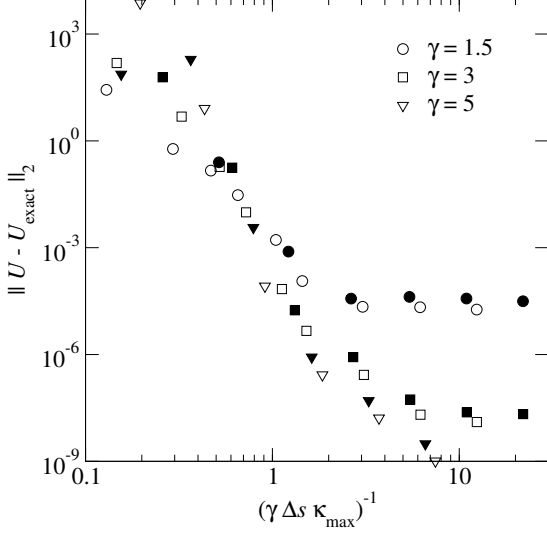
Figure 2: Surface velocity error for spheroids of aspect ratio 4 (open symbols) and 2 (closed symbols).

$\max[0, Y_j - \gamma \Delta s \, n_y(s_j)]$, where Δs is the local node spacing and γ is a parameter measuring the source's distance inside the boundary relative to Δs.

Figure 2 shows the surface velocity error for prolate spheroids of aspect ratio 2 and 4. The optimal value of γ depends on both the grid spacing, Δs, and the maximum curvature, κ_{max}. When $\gamma \Delta s \, \kappa_{max} \lesssim 1$, that is, when the radius of curvature is similar in magnitude to the offset distance of the ring sources, the error is large, independent of γ. For prolate spheroids and ellipses, the maximum curvature occurs at the nose and, in this implementation, some of the point or ring sources are forced onto the plane or axis of symmetry. More generally, it is reasonable to expect that the point/ring source techniques will experience difficulty whenever the radius of curvature becomes small in comparison to the offset distance of the sources.

Boundary-layer flow

Using the Görtler and (in the case of axisymmetric flow) Mangler transformations, the boundary-layer equations [5] reduce to

$$f_{\eta\eta\eta} + f f_{\eta\eta} + \beta(\xi)(1 - f_\eta^2) = 2\xi(f_\eta f_{\xi\eta} - f_\xi f_{\eta\eta}) \quad (10)$$

where

$$\eta = \frac{U(s)}{\nu\sqrt{2\xi}} n, \quad \psi(s,n) = \nu\sqrt{2\xi} f(\xi, \eta), \quad (11)$$

(s, n) are coordinates parallel and normal to the surface, respectively, $\psi(s, n)$ is the streamfunction, $U(s)$ is the local surface velocity obtained from the potential solution, ν is the kinematic viscosity, and subscripts on f denote differentation. For plane-symmetric flows,

$$\xi = \frac{1}{\nu}\int_0^s U(s)\,\mathrm{d}s \quad \text{and} \quad \beta(\xi) = 2\nu\frac{U'(s)}{U^2(s)}\xi. \quad (12)$$

For axisymmetric flows, the Mangler transformation is also applied, giving

$$\xi = \frac{1}{\nu}\int_0^s U(s)Y^2(s)\,\mathrm{d}s \quad \text{and} \quad \beta(\xi) = 2\nu\frac{U'(s)Y^2(s)}{U^2(s)}\xi. \quad (13)$$

Equation (10) is subject to the boundary conditions

$$f(0) = 0, \quad f_\eta(0) = 0, \quad \text{and} \quad f_\eta(\infty) = 1, \quad (14)$$

	Plane-symmetric		Axisymmetric	
	$\eta - f(\eta)$	$f_{\eta\eta}(0)$	$\eta - f(\eta)$	$f_{\eta\eta}(0)$
Box method	0.6480	1.2328	0.8046	0.9278
Schlichting [5]	0.6480	1.2326	0.8047	0.9277

Table 1: Boundary-layer solver validation for self-similar stagnation point flow. Note that $\eta - f(\eta)$ should be evaluated in the limit $\eta \to \infty$, but is here evaluated at $\eta = 5$.

and solved using the Keller Box method [5]. Second-order accurate finite difference and interpolation schemes are used to discretize (10) and a Newton method is used to solve the resulting nonlinear difference equations at each streamwise station. Adaptive Romberg integration is used to evaluate the integrals in (12) and (13). Second order finite differences are used to evaluate $U'(s) = \mathrm{d}U/\mathrm{d}s$. The far-field boundary condition is applied at $\eta = 5$. Consideration of plane-symmetric and axisymmetric stagnation point flow yields $\beta(0) = 1$ and $\beta(0) = 1/2$, respectively.

Table 1 compares published results for self-similar stagnation point flow with those calculated using the Box Scheme solver with 100 nodes. This is not a complete check of the solver because the right-hand-side of (10) vanishes for self-similar boundary-layer flows. For plane-symmetric flow past a circular cylinder, the combined potential and boundary-layer solvers predict a separation angle of $104.3°$, compared with a published value $104.5°$ [5]. For axisymmetric flow past a sphere, the combined potential and boundary-layer solvers predict a separation angle of $104.6°$, compared with published values in the range 103.6–$109.6°$[6]. These values are obtained using 100 nodes in both the circumferential and wall-normal directions and first-order interpolation between circumferential grid points.

Optimization

A discrete optimization problem is obtained by defining a discrete design or control vector, $\mathbf{x}$, whose components determine the forebody node positions according to

$$\mathbf{X}(s_i) = x_i \mathbf{n}_0(s_i) + \mathbf{X}_0(s_i), \quad i = 1, \ldots, M, \quad (15)$$

where x_i is the i-th component of $\mathbf{x}$, $\mathbf{n}_0$ and $\mathbf{X}_0$ are the normal and position vectors of a reference (initial) geometry, and M is the number of nodes on the forebody. Note that the objective function is still linear with respect to $\mathbf{x}$. The discrete constraints are

$$g_i(\mathbf{x}) = -\tau(s_i) \leq 0 \quad (16)$$

$$g_{i+M}(\mathbf{x}) = -X_s(s_i) \leq 0 \quad (17)$$

where $i = 1, \ldots, M$. Although there are $2M$ constraints, only a maximum of M can be active.

Using the boundary-layer solver described above, it is not possible to continue solutions downstream of the separation point due to the presence of the Goldstein singularity. It is therefore necessary to use an optimization algorithm that generates shape iterates that are always feasible, that is, unseparated. We use the Feasible Direction Interior Point (FDIP) method [2, 3]. With the above definitions, application of the algorithm to the present problem is straightforward.

The FDIP method is a gradient-based algorithm. For our problem, the objective function is linear, so analytical computation of $\nabla f(\mathbf{x})$ is trivial. Finite differences are used to compute $\nabla g_i(\mathbf{x})$. Although expensive, this is satisfactory for sufficiently small problems, such as those presented in this paper. The Lagrangian Hessian is set to the identity matrix, resulting in a first-order method. A smoothing operator is applied to updates to help preserve shape regularity [4].
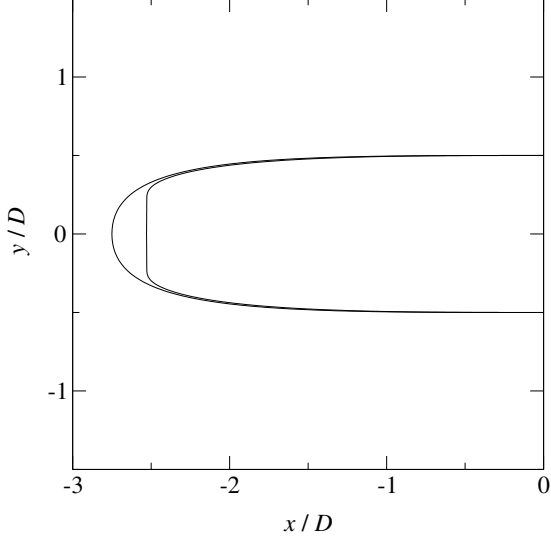
Figure 3: Initial and optimized forebody after 30 iterations for plane-symmetric flow.
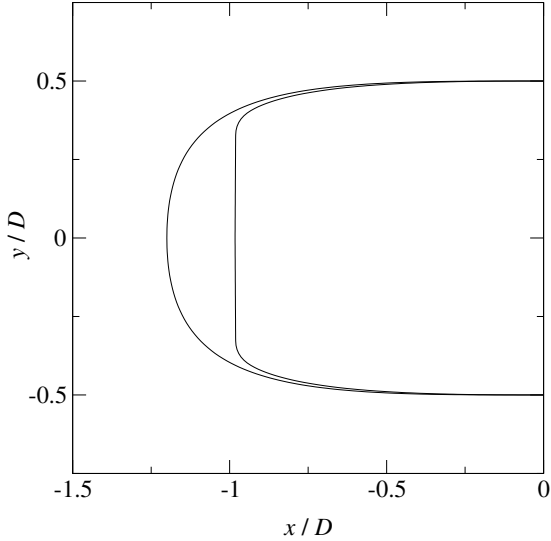

Figure 4: Initial and optimized forebody after 30 iterations for axisymmetric flow.

Results

Figures 3 and 4 show the initial and optimized shapes for plane-symmetric and axisymmetric flow, respectively. In each case, the initial forebody geometry is specified as the lowest order Chebyshev polynomials that satisfy $Y(0) = 0$, $Y(s_0) = D/2$, $Y_s(s_0) = 0$, $Y_{ss}(s_0) = 0$ and $X(0) = -L_{init}$, $X_s(0) = 0$, and $X(s_0) = 0$. L_{init} is chosen sufficiently large to obtain a feasible initial geometry. The results are obtained with $\gamma = 3$, $N = 800$, $M = 240$, $L_A/D = 8.56$ for the plane-symmetric case and $\gamma = 3$, $N = 400$, $M = 100$, and $L_A/D = 3.38$ for the axisymmetric case. Calculations are terminated when progress stalls, or when the curvature and shear stress profiles develop significant grid-scale oscillations. These features are rejected because they are not retained upon grid refinement.

Figures 5 and 6 show the pressure coefficient,

$$c_p \equiv \frac{p - p_\infty}{\frac{1}{2}\rho U_\infty^2} = 1 - \left(\frac{U}{U_\infty}\right)^2, \qquad (18)$$
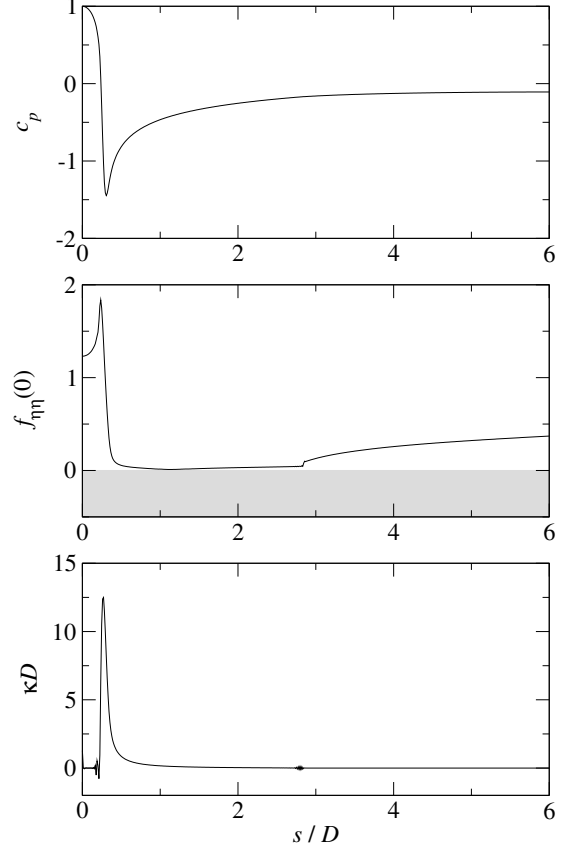

Figure 5: Pressure coefficient, shear stress, and curvature after 30 iterations in the plane-symmetric case. The junction is located at $s_0/D = 2.84$. The shaded area indicates separated (infeasible) solutions.

$f_{\eta\eta}$ evaluated at the wall ($\eta = 0$), and the curvature for the plane-symmetric and axisymmetric case, respectively. Note that at any streamwise station, $f_{\eta\eta}(0)$ is proportional to the wall shear stress, τ, and is a convenient nondimensional substitute. The maximum curvature, maximum shear stress, and minimum pressure coefficient are clearly correlated. The optimization algorithm drives the geometry towards an almost discontinuous curvature variation. This causes curvature overshoots, as the splines struggle to resolve such features. The optimal geometry consists of an essentially flat-plate stagnation-point flow with a favourable pressure gradient up to the point of maximum curvature. Between this point and the junction with the aftbody, an approximately zero shear-stress surface is obtained.

The effect of aftbody length, L_A, is shown in Figure 7. Upstream influence can only enter through the pressure coefficient. The plane-symmetric case is more sensitive to aftbody length than the axisymmetric case and there appears to be some residual effect at $L_A/D = 5.39$.

Discussion

The limitations of the flow solvers used in this paper are widely understood. Potential flow and first-order boundary-layer theory provide an accurate prediction when the Reynolds number is large and large-scale separation and transition do not occur. As the flow in the vicinity of the forebody is attached by design and separation occurs far downstream, we expect the present approximations to be qualitatively meaningful. Higher order effects, such as boundary-layer displacement effects, are ignored, as are the effects of instability and transition to turbulence that
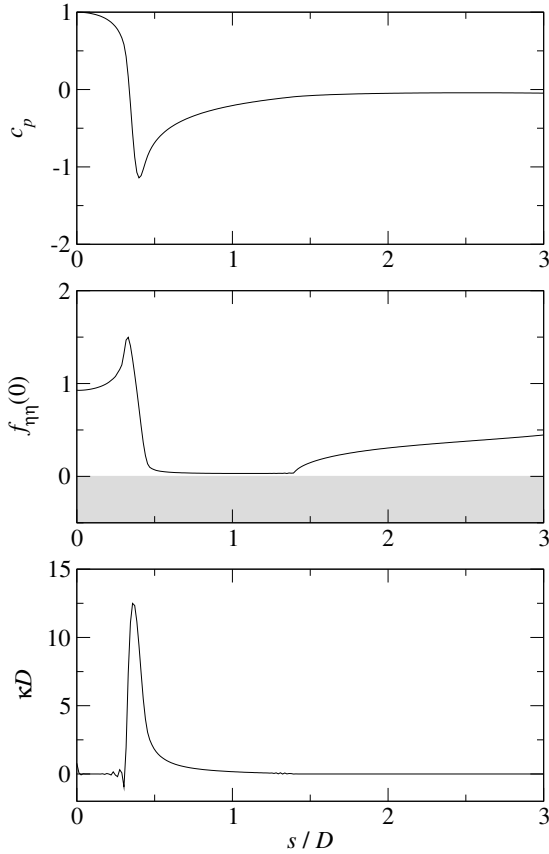
Figure 6: Pressure coefficient, shear stress, and curvature after 30 iterations in the axisymmetric case. The junction is located at $s_0/D = 1.39$. The shaded area indicates separated (infeasible) solutions.
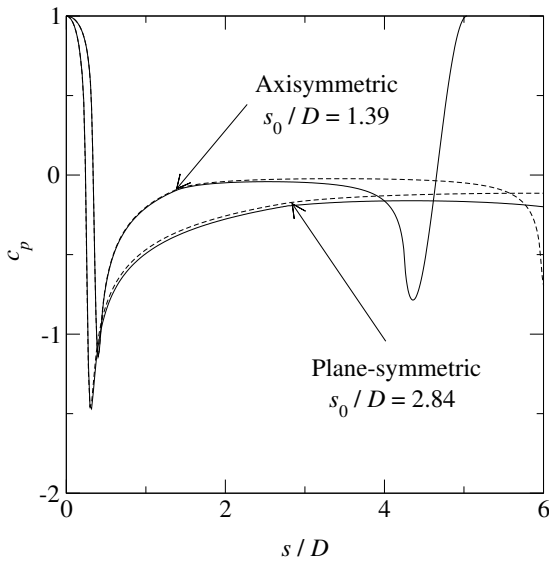

Figure 7: Effect of aftbody length on pressure coefficient profiles for plane-symmetric (solid line, $L_A/D = 5.39$; dashed line $L_A/D = 8.56$) and axisymmetric (solid line, $L_A/D = 3.38$; dashed line $L_A/D = 5.09$) cases.

will occur at sufficiently large Reynolds number. The zero shear stress surface is rather sensitive to perturbations in the geometry, suggesting that displacement effects may be important in a physical flow. The adverse pressure gradient associated with the zero shear stress surface implies the existence of an inflection point in the boundary-layer velocity profiles, hence the boundary layer will be particularly susceptible to instability. It is likely the forebody geometry will need to be modified to take these effects into account. This is the subject of future work.

Another important factor in the physical flow is sensitivity to angle of incidence. The optimized forebody geometries exhibit rather sharp corners. We expect that such features would promote separation in the presence of small angles of incidence. This is also the subject of future work.

The optimizing algorithm can find solutions of the discrete problem with lower values of the objective function than the examples shown here. Approaching these solutions, the shapes tend to lose regularity, with large oscillations in the curvature causing similar oscillations in the streamwise shear stress profiles. As mentioned above, such solutions are rejected, but a rational criterion for doing this has not been developed. As a result, it is not possible to be certain how well-converged the solutions are.

Conclusions

Classic flow solvers are combined with the FDIP optimization algorithm to obtain minimum-length forebody geometries free from separation. The optimal geometry consists of an essentially flat plate normal to the flow, connected to the aftbody by a smooth surface with almost zero shear stress. For the plane-symmetric case, the minimum forebody aspect-ratio was approximately 2.5, compared with approximately 1.0 for the axisymmetric case.

Acknowledgements

References

[1] Cao, Y., Schultz, W. W. & Beck, R. F., Three-dimensional desingularized boundary integral methods for potential problems, *Int. J. Numer. Meth. Fl.*, **12**, 1991, 785–803.

[2] Herskovits, J. & Santos, G., On the computer implementation of feasible direction interior point algorithms for nonlinear optimization, *Struct. Optimization*, **14**, 1997, 165–172.

[3] Herskovits, J., Feasible direction interior-point technique for nonlinear optimization, *J. Optimiz. Theory App.*, **99**, 1998, 121–146.

[4] Mohammadi, B. & Pironneau, O., *Applied Shape Optimization for Fluids*, Oxford University Press, Oxford, 2001.

[5] Schlichting, H. & Gersten, K., *Boundary Layer Theory*, Springer-Verlag, Berlin, 2000.

[6] White, F. M., *Viscous Fluid Flow*, McGraw-Hill, New York, 1974.